

# UC Irvine

## UC Irvine Previously Published Works

### Title

Deciphering Intrinsic Inter-subunit Couplings that Lead to Sequential Hydrolysis of F1-ATPase Ring

### Permalink

<https://escholarship.org/uc/item/5d96s8zk>

### Journal

Biophysical Journal, 113(7)

### ISSN

0006-3495

### Authors

Dai, Liqiang  
Flechsig, Holger  
Yu, Jin

### Publication Date

2017-10-01

### DOI

10.1016/j.bpj.2017.08.015

### Copyright Information

This work is made available under the terms of a Creative Commons Attribution License, available at <https://creativecommons.org/licenses/by/4.0/>

Peer reviewed

# Deciphering Intrinsic Inter-subunit Couplings that Lead to Sequential Hydrolysis of F<sub>1</sub>-ATPase Ring

Liqiang Dai,<sup>1</sup> Holger Flechsig,<sup>2</sup> and Jin Yu<sup>1,\*</sup>

<sup>1</sup>Complex System Research Division, Beijing Computational Science Research Center, Beijing, China and <sup>2</sup>Department of Mathematical and Life Sciences, Graduate School of Science, Hiroshima University, Hiroshima, Japan

**ABSTRACT** Rotary sequential hydrolysis of the metabolic machine F<sub>1</sub>-ATPase is a prominent manifestation of high coordination among multiple chemical sites in ring-shaped molecular machines, and it is also functionally essential for F<sub>1</sub> to tightly couple chemical reactions and central  $\gamma$ -shaft rotation. High-speed AFM experiments have identified that sequential hydrolysis is maintained in the F<sub>1</sub> stator ring even in the absence of the  $\gamma$ -rotor. To explore the origins of intrinsic sequential performance, we computationally investigated essential inter-subunit couplings on the hexameric ring of mitochondrial and bacterial F<sub>1</sub>. We first reproduced in stochastic Monte Carlo simulations the experimentally determined sequential hydrolysis schemes by kinetically imposing inter-subunit couplings and following subsequent tri-site ATP hydrolysis cycles on the F<sub>1</sub> ring. We found that the key couplings to support the sequential hydrolysis are those that accelerate neighbor-site ADP and Pi release upon a certain ATP binding or hydrolysis reaction. The kinetically identified couplings were then examined in atomistic molecular dynamics simulations at a coarse-grained level to reveal the underlying structural mechanisms. To do that, we enforced targeted conformational changes of ATP binding or hydrolysis to one chemical site on the F<sub>1</sub> ring and monitored the ensuing conformational responses of the neighboring sites using structure-based simulations. Notably, we found asymmetrical neighbor-site opening that facilitates ADP release upon enforced ATP binding. We also captured a complete charge-hopping process of the Pi release subsequent to enforced ATP hydrolysis in the neighbor site, confirming recent single-molecule analyses with regard to the role of ATP hydrolysis in F<sub>1</sub>. Our studies therefore elucidate both the coordinated chemical kinetics and structural dynamics mechanisms underpinning the sequential operation of the F<sub>1</sub> ring.

## INTRODUCTION

Coordination on ring-shaped NTPases is fundamental and crucial for the diverse physiological functions of these cellular molecular machines (1–5). In well-studied systems such as F<sub>0</sub>F<sub>1</sub>-ATP synthase, the binding-change mechanism, for example, was proposed early on to illustrate rotary cooperative catalysis around the hexameric F<sub>1</sub>-ATPase ring (6,7). The mechanism indicated that binding and catalytic activities of ATP alternate sequentially on three chemically active sites, formed at the interfaces of the  $\alpha$  and  $\beta$  subunits on the ring (8). According to the mechanism, the central  $\gamma$ -shaft across the F<sub>1</sub> ring dictates the coordinated alternation (9–12). Nevertheless, experimental studies later on showed that upon significant truncations of the  $\gamma$ -shaft, the F<sub>1</sub> motor still rotates directionally (13–16). Furthermore, recent experiments conducted in the absence of the central  $\gamma$ -shaft demonstrated that the stator F<sub>1</sub>-ring also maintains

rotary sequential hydrolysis around the three chemical sites (17). These studies consistently indicated that the sequential coordination arises intrinsically from the F<sub>1</sub>-ATPase ring, though the stator-rotor interactions would likely enhance the rotary cooperativity.

In this work, we aimed to investigate how the intrinsic sequential operation on the F<sub>1</sub> ring arises due to inter-subunit or site couplings in the absence of the central  $\gamma$ -shaft. We assume that the sequential hydrolysis scheme achieved without the  $\gamma$ -rotor is similar to that detected originally with the rotor. We focused on two typical reaction schemes, one suggested recently for human mitochondrial F<sub>1</sub> (MF<sub>1</sub>) (18), and the other determined for bacterial F<sub>1</sub> (BF<sub>1</sub>) (19). For an individual ATPase site, formed by one  $\alpha$ - $\beta$  heterodimer, the uni-site reaction rates for the product ADP and Pi releases, for example, are particularly low (20,21). To allow reactions that are as fast as that achieved on the tri-site F<sub>1</sub> ring, it is necessary that the inter-subunit couplings significantly accelerate the respective product releases, yet how that is achieved remains elusive. Inter-subunit coordination has been recognized in particular for ring-like

Submitted March 2, 2017, and accepted for publication August 4, 2017.

\*Correspondence: [jinyu@csrc.ac.cn](mailto:jinyu@csrc.ac.cn)

Editor: Hiroyuki Noji.

<http://dx.doi.org/10.1016/j.bpj.2017.08.015>

© 2017 Biophysical Society.

This is an open access article under the CC BY-NC-ND license (<http://creativecommons.org/licenses/by-nc-nd/4.0/>).

NTPases (1,2,22), such as the viral RNA or DNA packaging motor (23,24), helicases (4,5,25), and F<sub>1</sub>-ATPase (2,6,26). For example, in the viral  $\phi$ 29 DNA packaging motor, it was discovered that multiple subunits coordinate ADP release with ATP binding in an alternating fashion during a packaging dwell phase (1,24,27), whereas Pi release happens from one site to the next in a burst phase. Nevertheless, it is not clear what inter-subunit interactions support the coordination, and similar puzzles remain for various ring-shaped NTPases. Some suggestions have been made that address, for example, how ATP binding in one site may couple with ADP release in a neighbor site (1,24,26,27), how an arginine-finger insertion from one subunit can induce ATP hydrolysis in the next-neighbor site (23,24,27), and how ATP hydrolysis may assist Pi release in the neighbor site (28) or vice versa. A basic scenario is that one chemical event triggers certain conformational changes that propagate through the subunit interfaces to the neighbor site(s), accelerating the site conformational transitions on the forward chemical reaction path, with both kinetic and structural consequences. However, quantitative studies to reveal these couplings and determine the underlying kinetics or structural dynamics are lacking.

Accordingly, the major task of this study is to identify the inter-subunit couplings that essentially support the sequential hydrolysis of the F<sub>1</sub> stator ring, along with quantitative descriptions and physical understanding. Computational modeling and simulations have contributed significantly to the understanding of molecular mechanisms of F<sub>1</sub>-ATPase (29–38). Although most previous computational studies have focused on quantifying the rotary motion of F<sub>1</sub>-ATPase ( $\alpha_3\beta_3\gamma$ ), current work has neglected the rotational degree of freedom and studied only a minimal model of the F<sub>1</sub> ring ( $\alpha_3\beta_3$ ) for sequential hydrolysis. We started by conducting stochastic kinetics simulations for the three independent ATP hydrolysis cycles, based on the uni-site reaction rates obtained for bovine heart MF<sub>1</sub> (21) and *Escherichia coli* F<sub>1</sub> (20). Empirically chosen inter-site couplings that are likely to happen upon assembly and operation of the ring were then kinetically incorporated into the stochastic simulation, and the kinetic rates were tuned, in particular, under a constant free-energy condition for ring operation. If a sequential hydrolysis reaction arises in the tri-site reaction as experimentally detected under these couplings, we then regard the couplings as kinetically feasible.

For the kinetically feasible inter-subunit couplings that were identified as key for sequential hydrolysis, we then probed the physical basis of the couplings with structural dynamics investigations. Previously, atomistic molecular dynamics (MD) simulation studies had been performed on the F<sub>1</sub>-ATPase system to reveal protein conformation changes from several nanoseconds (30) to tens and hundreds of nanoseconds (37). Nevertheless, micro- to millisecond “long-timescale” dynamics in such a protein machine is still hardly accessible for conventional MD simulations. As

mentioned above, the inter-subunit couplings are usually manifested as the neighbor-site conformational responses toward an active site where some triggering chemical event, such as ATP binding or hydrolysis, happens, with a “waiting time” up to milliseconds or above. To allow such a “slow” event to happen in the MD simulation, we accordingly enforced conformational transitions to mimic the ATP binding or hydrolysis event in the corresponding active site by implementing targeted MD (TMD) in sub-microseconds (39–41). However, the purpose is not to simulate the triggering event per se, but to monitor the ensuing conformational relaxations or responses on the ring. Considering that artifacts or bias might be introduced in the highly accelerated sub-microsecond TMD, we additionally performed coarse-grained (CG) simulations with similar enforcing and relaxation strategies, since CG simulations are supposed to capture comparatively slow motions. As the essential conformational responses appearing in the accelerated atomistic MD simulation could be reproduced on the CG level connecting to the long timescale, the TMD-induced responses are regarded to be as reasonable as those that happen without acceleration.

In practice, we adopted a reaction scenario in which Pi is released after the ADP release in one hydrolysis cycle of F<sub>1</sub> (19,42). Using stochastic kinetic simulations, we were able to first determine kinetically feasible inter-subunit couplings that support the sequential hydrolysis. Then, we implemented atomistic MD simulations to probe the physical basis of the kinetically important couplings. The bovine MF<sub>1</sub> structure was employed in the MD simulation. Once the TMD was implemented to mimic ATP binding or hydrolysis in one active site, the conformational responses in both neighbor sites were closely monitored. We subsequently found asymmetrical neighbor-site openings that may facilitate the product(s) release or bias the ATP binding for directional coordination. To validate the TMD implementation to a comparatively long timescale, we further implemented targeted elastic network (TEN) simulations in a CG structural model.

## METHODS

### Kinetic Monte Carlo simulation of three chemical sites

For each ATP binding or catalytic site at the  $\alpha$ - $\beta$  interface, there are several chemical states: the empty state without any substrate binding (E); the ATP-bound state and the hydrolysis-ready state (T/T\*); the post-hydrolysis state right after the reaction, as ATP turns into ADP and Pi (DP); and the ADP-released but Pi-bound state (P). Here, we follow the convention that the ADP releases before the Pi release (19,42). As such, the uni-site reaction proceeds in cycles as  $E \rightleftharpoons T/T^* \rightleftharpoons DP \rightleftharpoons P \rightleftharpoons E$ . We differentiate T\* from T by enhancing the ATP-hydrolysis rate of the T\*-state above that of the T-state, as if T\* arises due to the assembly of the tri-site ring.

The uni-site reaction rates for forward and backward transitions in the bovine heart mitochondrial and bacterial *E. coli* F<sub>1</sub>-ATPase were obtained experimentally (20,21) (see Tables S1 and S2). We assume that the rate

of ADP release from the DP state is the same as that originally listed from the D state, and the rate of Pi release from the P state is the same as that originally listed from the DP state. We also assume that bovine and human MF<sub>1</sub> behave similarly (18), and that *E. coli* and thermophilic (*Bacillus PS3*) BF<sub>1</sub> perform alike as well (43).

We used the kinetic Monte Carlo (KMC) method (44) to simulate the chemical kinetics of F<sub>1</sub>-ATPase hydrolysis, from the three independent uni-site reactions to the coupled tri-site reactions. In the KMC simulation, one starts with an initial ring configuration (e.g., E-E-E or E-DP-T) of the three chemical sites; each time a transition from one of the three chemical sites was made, either forward or backward along the reaction path, according to rate competitions of all potential transitions in the current ring configuration (i.e., fast transitions get higher chances). When the uni-site reaction rates were adopted for each site, the three sites performed as if they hydrolyzed independently. In any coupled tri-site reaction scheme, inter-subunit couplings were imposed at certain ring configurations, for example, by tuning the product-release rates upon neighbor-site ATP binding (E→T) or hydrolysis reaction (T\*→DP). In particular, we used four parameters to define the strength of the couplings, and we tuned these parameters for optimal sequential performance (see the [Supporting Material](#)).

## Atomistic TMD simulations

All the MD simulations were performed using the NAMD 2.10 software (45) with the CHARMM22 force field for protein and the CHARMM27 force field for lipid (46,47), except for the construction of the E-DP-T structure, for which GROMACS was used (48). The F<sub>1</sub>-ATPase structures were obtained from the existing crystal structures: The E-DP-T ring was made from the crystal structure of P-DP-T (Protein Data Bank (PDB): 1E1R) (49); the  $\gamma$ -shaft, when included, was rotated  $\sim 40^\circ$  accordingly. An E-T-T\* structure was obtained directly from the crystal structure (PDB: 2JDI) (50). An E-E-E structure was made from E-T-T, and a T-P-T\* structure was obtained from the crystal structure (PDB: 1W0J) (51) (see the [Supporting Material](#)).

The PDB structures were then solvated with TIP3P water in a cubic box, and the minimum distance from the protein to the wall was 15 Å. We neutralized the systems with Na<sup>+</sup> and Cl<sup>-</sup> to a concentration of 0.15 M. The temperature was set to 310 K and the pressure was 1 bar. The van der Waals and short-range electrostatic interactions used a cutoff of 12 Å. The particle-mesh Ewald method was applied to deal with long-range electrostatic interactions (52). The solvated system was minimized with the steepest-descent algorithm, followed by a 10 ps MD simulation under the canonical ensemble with a time step of 1 fs. Then, a 5 ns equilibrium simulation was performed under the NVT ensemble with a time step of 1 fs, and position restraints were imposed on the heavy atoms of proteins during the simulation. After the constrained simulation, the unconstrained equilibrium simulations, or TMD simulations, were carried out under the NPT ensemble with a time step of 2 fs. During the TMD simulation, the structure was constantly forced toward a moving target conformation (according to the heavy-atom root mean-square deviation (RMSD) value) geometrically designated on the reaction path toward a final target structure (39). Further implementations are found in the [Supporting Material](#).

## Performing the elastic-network relaxation dynamics

The elastic network of the ring was obtained by first replacing each amino acid residue in the atomic structure by a single bead, which was placed at the position of the  $\alpha$ -carbon atom of the respective residue. These equilibrium positions were denoted by  $\vec{R}_i^{(0)}$  for bead  $i$ . Then, to determine the pattern of network connections, the distances  $d_{ij}^{(0)} = |\vec{R}_i^{(0)} - \vec{R}_j^{(0)}|$  between equilibrium positions of any two beads  $i$  and  $j$  were compared with a prescribed interaction radius  $r_{int} = 10\text{Å}$ . If this distance was below  $r_{int}$ , the

two beads were connected by a deformable elastic spring with natural length  $d_{ij}^{(0)}$ . The network connectivity was stored in matrix  $A$  with entries  $A_{ij} = 1$ , if beads  $i$  and  $j$  are connected, and  $A_{ij} = 0$ , else. The total elastic energy of the network is  $U = \sum_{i,j:i < j} \kappa (A_{ij}/2)(d_{ij} - d_{ij}^{(0)})^2$ . Here,  $N$  is the number of beads in the protein network,  $d_{ij} = |\vec{R}_i - \vec{R}_j|$  is the actual length of a spring connecting beads  $i$  and  $j$  in some deformed network conformation, with  $\vec{R}_i$  being the actual position vector of bead  $i$ , and  $d_{ij}^{(0)}$  is the corresponding natural length. The spring stiffness constant  $\kappa$  is assumed to be the same for all network springs.

When thermal fluctuations and hydrodynamical interactions are neglected, the dynamics of the network can be described by a set of Newton's equations in the over-damped limit (53–55). For bead  $i$  the equation of motion is

$$\gamma \frac{d\vec{R}_i}{dt} = -\frac{\partial}{\partial \vec{R}_i} U. \quad (1)$$

On the left side of Eq. 1,  $\gamma$  is the friction coefficient assumed to be equal for all network beads. On the right side are the elastic forces exerted by network springs of beads which are connected to bead  $i$ . Explicitly, the equations read

$$\frac{d\vec{R}_i}{dt} = -\sum_j A_{ij} \frac{d_{ij} - d_{ij}^{(0)}}{d_{ij}} (\vec{R}_i - \vec{R}_j) + \vec{f}_i. \quad (2)$$

Here, we have removed the dependencies on  $\gamma$  and  $\kappa$  by an appropriate rescaling of time and, after that, added external forces  $\vec{f}_i$  which can act on bead  $i$  (if  $\sigma = 1$ ).

In the TEN simulations performed, external forces were applied only to the beads of one of the catalytic  $\alpha\beta$ -sites to induce the desired transition there. Such forces were updated in each integration step and had the form  $\vec{f}_{i,n} = (\alpha/N_s) |\text{RMSD}_{n-1} - \text{RMSD}^*| \vec{d}_{i,n-1}$ , for bead  $i$ . Here,  $\vec{d}_{i,n}$  is the difference vector between positions of bead  $i$  in the target and the actual conformation of the forced  $\alpha\beta$ -subunit, determined after superposition of the subunits at integration step  $n$ , and  $\text{RMSD}^* = \text{RMSD}_0 - \text{RMSD}_0(n/S)$ , with  $S$  being the total number of integration steps.  $N_s$  is the number of beads of the forced  $\alpha\beta$ -subunit, and parameters  $\alpha = 2500$  and  $S = 400,000$  were chosen in the simulations. The set of Eq. 2 was numerically integrated to obtain the positions of network beads at all moments in time. In the simulations, a first-order scheme with a time step of 0.1 was used. In particular, we performed TEN to mimic ATP binding to the E-site of the E-DP-T ring, in comparison with the TMD simulation. Further details can be found in the [Supporting Material](#).

## RESULTS

### Stochastic simulations identified kinetically feasible inter-subunit couplings that support sequential hydrolysis on the F<sub>1</sub> ring

To probe what type of inter-subunit or site couplings may be responsible for sequential hydrolysis of the F<sub>1</sub> ring, we first conducted the kinetic Monte Carlo (KMC) simulations for three ATP hydrolysis cycles to mimic the chemical kinetics of the three active sites (see Fig. 1; [Methods](#)). The three chemical cycles proceed independently when there is no inter-subunit coupling. The coordinated sequential hydrolysis arises kinetically when certain transitions in one hydrolysis cycle are connected with those in another hydrolysis cycle at the right moments via appropriate coupling rules (see [Supporting Material](#)).

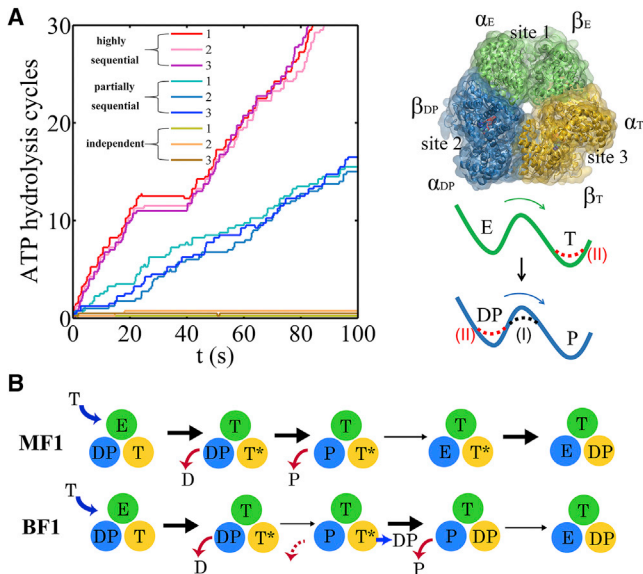


**FIGURE 1** Stochastic simulations of tri-site hydrolysis reactions on the F<sub>1</sub> ring. (A) The trajectories (*left*) show the number of hydrolysis cycles for the three chemical sites of BF<sub>1</sub>, from the independent (*yellow traces*, with three different shades shown for the three active sites) to the partially coordinated (*blue traces* with three shades) and the highly sequential case (*red traces* with three shades). In the sequential case, each site follows its upstream/counterclockwise site along the ATP hydrolysis reaction path, as detected experimentally. In the independent case, the uni-site reaction rates from *E. coli* F<sub>1</sub> were used (20). The ring-shaped structure (*right*) of a key configuration, E-DP-T, is shown (E for the empty state, T for the ATP bound state, DP for the ADP+Pi or the hydrolysis state, and P for the Pi bound state), with the most essential inter-subunit coupling illustrated: ATP binding to the E-site facilitates ADP release from the next DP-site. The coupling is imposed in two ways, implementations I and II (see text). Implementation I was used for the BF<sub>1</sub> trajectories shown here. (B) The sequential hydrolysis schemes for MF<sub>1</sub> (*top*) and BF<sub>1</sub> (*bottom*), with the essential inter-subunit couplings enabling the schemes indicated. The ATP binding (E→T) to E-DP-T enhances the ADP release (DP→P) for both MF<sub>1</sub> and BF<sub>1</sub>; in MF<sub>1</sub>, Pi release (P→E) is enhanced right after the ADP release upon ATP binding, whereas in BF<sub>1</sub>, Pi release is enhanced either similarly to that in MF<sub>1</sub> and/or later, upon ATP hydrolysis (T\*→DP). To see this figure in color, go online.

We started by simulating the three independent hydrolysis cycles based on the uni-site reaction rates obtained experimentally, for both MF<sub>1</sub> and BF<sub>1</sub> (20,21) (see [Tables S1](#) and [S2](#)). Each hydrolysis cycle consists of ATP binding (from E, the empty state, to T, the ATP-bound state), hydrolysis (T or T\* to DP, the ADP+Pi bound state), and product release (DP to P, the Pi-bound state, and then to E). We then imposed coupling rules onto the three ATP hydrolysis cycles in the KMC simulations ([Fig. S1](#)). First, since the three-ATP-bound configuration (3-T) was not detected experimentally (17), we imposed a constraint to prevent 3-T when needed by lowering the third ATP binding rate to the ring (e.g., for ~100 times the rate inhibition; see [Figs. S1, S2, and S3](#)). It turns out that MF<sub>1</sub> explicitly requires the constraint to achieve the sequential performance, since on the dominant reaction path of MF<sub>1</sub> (see [Fig. 1 B](#)), a

T-E-T\* configuration exists that readily turns into 3-T, which can then obtain a large population in the absence of the constraint (e.g., >60%). In BF<sub>1</sub>, however, the sequential performance was acceptable without adding the constraint, and the 3-T population would not become dominant (i.e., it remained at <30%). Second, when two sites among the three are bound with ATP, we refer to the T\*-site as the one that binds ATP earlier, so that it proceeds to an intermediate T\* state (or tightly bound state, as in the assembled ring), ready for catalysis (31). We accordingly assigned an elevated ATP hydrolysis rate (e.g., ~100-fold rate enhancement; see [Figs. S1, S2, S3, and S4](#)) for the T\*-site.

Note that sequential performance was evaluated by a performance score (between 0 and 1), according to the experimentally detected sequential schemes (18,19). A higher score shows a better sequential performance or consistency with the detected scheme (see Eq. S1 in [Supporting Materials and Methods](#); [Figs. S2, S3, and S4](#)). In the case of a high score, one can consistently see high correlations between neighboring sites in their hydrolysis cycles, as one site follows the other closely moving along the hydrolysis reaction path (see Eq. S2 in [Supporting Materials and Methods](#); [Fig. S5](#)).

Representative trajectories for the ATP hydrolysis cycles on the three active sites of the BF<sub>1</sub> ring are shown in [Fig. 1 A](#), from an independent case to a partially coordinated and then a highly sequential case. In particular, the highly sequential case demonstrates an overall cycling rate (~0.3 s<sup>-1</sup>) comparable to the experimental detection on the rotor-less BF<sub>1</sub> (17). In the full F<sub>1</sub> in the presence of the central rotor, the cycling rates become hundreds to thousands times faster (18,43).

Since it is not clear whether product binding affinities change during the inter-subunit coupling, we imposed the coupling kinetically in two ways (see [Fig. 1 A, right](#)): For implementation I, we enhanced both the product unbinding and binding rates by the same amount to keep a constant binding affinity. For implementation II, we enhanced the product unbinding rate without changing the product rebinding rate, whereas the ATP unbinding rate or the reversal rate of the hydrolysis in the triggering active site was additionally enhanced to keep the overall free energy constant. The trajectories for MF<sub>1</sub> and BF<sub>1</sub> with both implementations I and II are shown in [Fig. S6](#). Regardless of the means of implementation, we found that the key couplings that support the sequential schemes are the same as those summarized below.

#### *ATP binding to the E-DP-T ring facilitates product release from the downstream DP site*

Presumably, as ATP binding (E→T) induces an open-to-closed transition in the E-site, the next downstream DP-site (in the counterclockwise direction viewed from the C-terminal side of F<sub>1</sub>) can be disturbed and the product (ADP and Pi) release rate can be affected (1,24,26). Accordingly, in the



kinetic simulation, we allowed the ATP binding to the E-DP-T ring to enhance both the ADP and Pi release rates in the DP-site. In MF<sub>1</sub>,  $>\sim 10^5$ -fold rate enhancement (see Fig. S3) was applied to both the ADP and Pi release (from E-DP-T to T-E-T\*) to achieve a high sequential performance. In BF<sub>1</sub> (from E-DP-T to T-P-DP), the ADP release rate has to be enhanced  $> 10^3$ -fold upon the E-site ATP binding (see Fig. S4) to allow the sequential performance; the Pi release rate either can be enhanced along with ADP release upon ATP binding or can occur after T\*-site ATP hydrolysis (see Fig. S2, B and C), as analyzed below.

*The Pi release from the T-P-T\* ring can be facilitated either by the upstream-site ATP binding or later by the downstream-site ATP hydrolysis*

Based on time-series data analyses from high-speed single-molecule experiments, it was suggested that ATP hydrolysis plays a role in facilitating the neighbor-site Pi release (28). We tested whether this causality coupling between ATP hydrolysis and Pi release could be kinetically feasible, i.e., to support sequential hydrolysis in the KMC simulation. We then found that in BF<sub>1</sub>, by enhancing the Pi release rate  $\sim 10^3$ -fold upon ATP hydrolysis in the next T\*-site (see Fig. S4), sequential hydrolysis could emerge. Alternatively, Pi release in BF<sub>1</sub> can also be enhanced right after ADP release, as in MF<sub>1</sub>, to support the sequential performance.

Note that the overall hydrolysis or cycling rates of F<sub>1</sub> achieved in our KMC simulations are comparatively low, e.g., less than one cycle (with three ATPs hydrolyzed) per second, as experimentally detected for BF<sub>1</sub> in the absence of the rotor (17). One can also enhance the coupling strengths to mimic the full F<sub>1</sub> system in the presence of the rotor to achieve high rates, i.e., up to hundreds of cycles per second, as measured for the full F<sub>1</sub> (18,43). The corresponding kinetic coupling parameters to achieve the low and high rates of F<sub>1</sub> are provided in Tables S3 and S4 for MF<sub>1</sub> and BF<sub>1</sub>, respectively.

In brief, from a kinetic perspective, the ATP-binding-facilitated ADP release in the downstream DP-site appears to be an indispensable coupling for sequential performance for both the MF<sub>1</sub> and BF<sub>1</sub> rings. On the other hand, the coupling for promoting Pi release could be attributed either to ATP binding in the upstream site (in MF<sub>1</sub>), or to ATP hydrolysis in the downstream T\*-site, or both (in BF<sub>1</sub>). To further probe the physical basis of these kinetically feasible couplings, we performed atomistic MD simulations as illustrated below.

### Atomistic MD simulations demonstrated an asymmetrical opening of the neighbor site upon current-site closing/tightening induced by ATP binding/hydrolysis

We performed four sets of TMD simulations (39) mimicking ATP binding or ATP hydrolysis in one chemical site, and we

monitored the ensuing mechanical responses from the two neighboring chemical sites. The four sets of simulations include 1) targeting the ATP-binding transition from E-DP-T to T-DP-T\* to examine how the downstream DP-site and the upstream T-site are affected, with a control TMD simulation to include the central  $\gamma$ -shaft; 2) targeting the ATP hydrolysis transition from T-P-T\* to T-P-DP to examine how the upstream P-site and downstream T-site react; 3) targeting the first-ATP binding transition from E-E-E to E-T-E to examine the responses without ligand bound in the neighbor sites; and 4) targeting the third-ATP binding transition to E-T\*-T, to see if the 3-T ring remains stable.

*ATP binding to the E-DP-T ring opens the downstream DP-site to facilitate ADP release*

We obtained an E-DP-T ring from the P-DP-T structure of bovine MF<sub>1</sub> (PDB: 1E1R) (49) and performed the TMD simulation to enforce the  $\alpha_E$ - $\beta_E$  structure to approach the targeted  $\alpha_T$ - $\beta_T$  conformation, so that the original E-site was turned into a T-site and a T-DP-T\* ring was obtained (see Fig. 2; Supporting Material, section II.4).

To determine whether the ATP binding site transitioned from open to closed as it was enforced to do, we calculated the C-terminal protrusion (i.e., on the DELSEED motif) height, the hinge-bending angle on the  $\beta$ -subunit, and the size of the ATP binding pocket (see Fig. S7). Large values of these measures indicate an open form, whereas small values indicate a closed one. In Fig. 2 A, we see that the  $\beta_E$ -protrusion decreased by  $\sim 6$  Å during the TMD simulation, indicating clearly a transition from an open site to a closed one (E  $\rightarrow$  T). In response, the average  $\beta_{DP}$  protrusion height increased slightly (by  $\sim 1$  Å; also see Fig. 2 B) and the  $\beta_{DP}$  hinge-bending angle also increased (by  $\sim 3^\circ$ ), accompanied by a small increase in the pocket size ( $\sim 0.2$  Å; see Fig. S8), all indicating a slight opening of the DP-site compared with the results from an equilibrium control simulation. In comparison, the average  $\beta_T$ -protrusion height decreased a little ( $\sim 1$  Å), though the pocket size of the T-site increased a bit ( $\sim 0.2$  Å), and the hinge-bending angle of  $\beta_T$  increased slightly ( $\sim 1^\circ$ ). Movies made from the simulation show both top and side views of the ring, highlighting how the  $\beta$ -protrusions shifted (Movies S1 and S2).

Since the average magnitudes of the responses were small, we performed an additional TMD simulation for the control, retaining the  $\gamma$ -shaft in the center of the E-DP-T ring. The average  $\beta_{DP}$  protrusion then increased to  $\sim 2$  Å upon the E-site closing (see Fig. S9), whereas the pocket size only increased in the downstream site but decreased in the upstream site. In brief, all three geometric measures consistently suggested that the downstream DP-site opened in response to the ATP binding in the E-site, whereas the upstream T-site did not show such an opening tendency. In particular, one could see that the DELSEED of  $\beta_{E \rightarrow T}$  moved toward the center of the ring during the enforced transition (see Fig. 2 C). The trend was maintained in

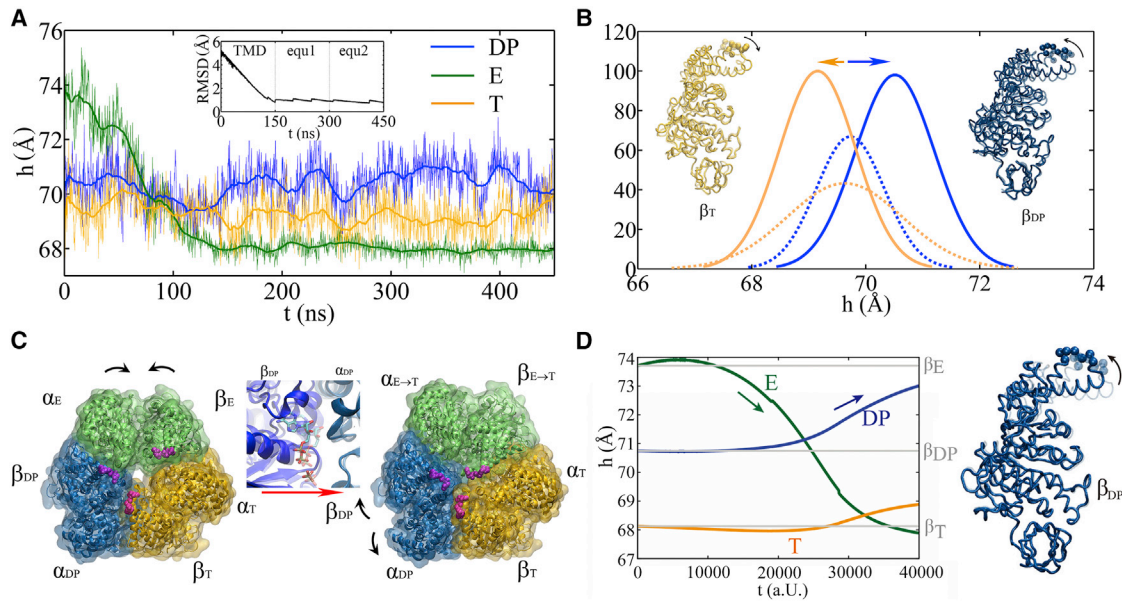


**FIGURE 2** The TMD simulation enforcing an ATP binding to the E-site in the E-DP-T ring. (A) In the first 150 ns TMD simulation, the E→T transition was gradually enforced; additional simulations were conducted for relaxation as holding the structure toward the final targeted form. The conformational changes of the chemical sites were monitored by the C-terminal protrusions of the  $\beta$ -subunits (green, E-site; blue, DP-site; yellow, T-site). (Inset) RMSD of  $\alpha_E$ - $\beta_E$  dimer with respect to the targeted  $\alpha_T$ - $\beta_T$ . (B) Histograms of the protrusion heights from  $\beta_{DP}$  (blue lines) and  $\beta_T$  (yellow lines) measured from the TMD simulations (solid curves) and the equilibration simulation in control (dashed curves), respectively (with the average changes indicated by arrows). Side views of the conformational changes on the  $\beta_T$  and  $\beta_{DP}$  C-terminal protrusions are shown, with spheres indicating the DELSEED motif (with the initial conformation in transparent ribbon and the final in non-transparent ribbon aligned together). (C) Top view from the C-terminal side of the F<sub>1</sub> ring, for both the initial (E-DP-T; left) and the final enforced configurations (T-DP-T\*; right). The DELSEED motifs are highlighted in magenta spheres. The widening of the DP-site interface between  $\alpha_{DP}$  and  $\beta_{DP}$  is also shown in the middle. The initial and final structures are aligned together and are shown in transparent and non-transparent representations, respectively, with  $\beta_{DP}$  colored blue,  $\alpha_{DP}$  colored light blue, and ADP/Pi in stick representation. (D) Results from the TEN simulations of the E-DP-T ring, with the protrusion changes of three sites shown on the left and the structural changes of the downstream  $\beta_{DP}$  subunit (with the initial in transparent ribbon and the final in non-transparent ribbon aligned together) shown on the right. To see this figure in color, go online.

the presence of the  $\gamma$ -shaft, though the  $\gamma$ -shaft occupancy prevents the  $\beta_{E\rightarrow T}$  protrusion from interacting directly with that of  $\beta_{DP}$ , and the  $\beta_{DP}$  protrusion then increased, largely due to the  $\gamma$ -shaft rotation.

Notably, even without the  $\gamma$ -shaft, one still sees that the DP-site interface widens between  $\alpha_{DP}$  and  $\beta_{DP}$  upon the enforced ATP binding (see Fig. 2 C). The conformational changes are actually quite significant in the peripheral region of the DP-site (within 10 Å of the bound ADP), with an RMSD of  $\sim 3$  Å upon the enforced transition (see Fig. S10 A). The average number of hydrogen bonds in that region also decreased (from  $\sim 25$  in the equilibrium MD to  $\sim 20$  in the TMD simulation; see Fig. S10 B). In particular, the hydrogen bonds that connect  $\alpha_{DP}$  and  $\beta_{DP}$  and ones on the  $\beta$ -strand of  $\alpha_{DP}$  frequently broke in the TMD simulation, but not in the equilibrium control simulation. All these features indicate an enlarging of the DP-site interface in response to the enforced ATP binding to the E-site.

To further probe how the DP-site region was able to respond to the enforced E-site to facilitate the ADP release, we also conducted steered MD (SMD) simulations to pull ADP out of the DP-site from the initial E-DP-T ring (before the TMD) and from the final T-DP-T\* structure (after the TMD), respectively. Three directions were chosen for the

ADP pulling: upward from the top of the DP bound pocket, and outward from and inward to the center of the ring. Correspondingly, we conducted three SMD simulations for each direction, to both the E-DP-T and T-DP-T\* rings before and after the TMD simulations ( $3 \times 3 \times 2 = 18$  SMD simulations; see Fig. S11; Supporting Material, section II.4). The results show that after the TMD simulation or the E-site closing, it was comparatively easy to pull the ADP out of the DP-site, and the contrast was made apparent for pulling along the upward and/or outside pathways. Close inspections along the steered ADP release paths show some structural clues as to how the release could possibly proceed (see Fig. S11).

Finally, we probed how the mechanical responses propagate from the ATP-binding E-site to the respective DP- and T-site in the stator F<sub>1</sub>-ring, without the  $\gamma$ -shaft. We calculated individual residue correlations with the E-site ATP-binding residues ( $\alpha I343$ ,  $\alpha R373$ ,  $\beta G161$ -V164,  $\beta Y345$ ,  $\beta A421$ ,  $\beta F424$ , and  $\beta T425$ ), which are mainly on the  $\beta_E$  subunit (see Fig. 3 A) by first evaluating the pairwise cross-correlation values for all residues (see Fig. S12) and then summing up the correlation strengths between each protein residue and those E-site ATP-binding residues. Close to the E-site, the correlations generated were similarly

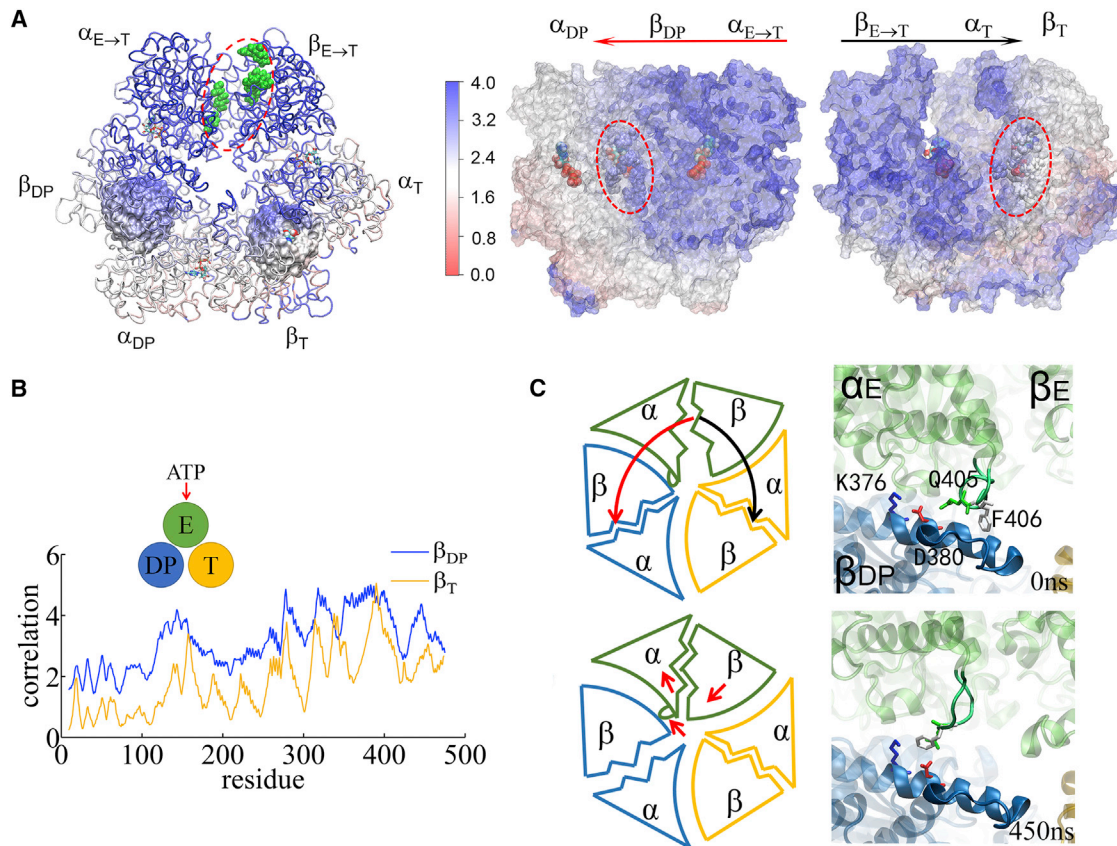


FIGURE 3 Conformation correlation with the ATP-binding-pocket residues in the TMD simulation of the E-DP-T ring. (A) Correlation map of the full ring during the enforced E→T transition starting from E-DP-T, colored according to correlation values (blue/white/red, high/medium/low) between individual residues and the E-site ATP binding residues (green spheres in the top view on the left). An inside view (right) shows the conformation propagation or correlation from  $\alpha_{E\rightarrow T}$  to  $\beta_{DP}$  and to  $\alpha_{DP}$  (left), and from  $\beta_{E\rightarrow T}$  to  $\alpha_T$  and to  $\beta_T$  (right), with the bound ADP+Pi and ATP at the DP-site and the T-site, respectively, circled. (B) The residue-wise correlation from  $\beta_{DP}$  (blue) and  $\beta_T$  (yellow). (C) A close inspection of the C-terminal region of  $\alpha_{E\rightarrow T}$  to  $\beta_{DP}$  during the TMD simulation is shown, with cartoon schematics on the left and zoom-in structural views on the right. To see this figure in color, go online.

high across  $\alpha_{E\rightarrow T}$  and  $\beta_{E\rightarrow T}$ , respectively (see Fig. 3 A, right). The correlation was still maintained high as being propagated from  $\alpha_{E\rightarrow T}$  to  $\beta_{DP}$  owing to an  $\alpha$ -loop region ( $\alpha$ Q405–D411) on the top of  $\alpha_{E\rightarrow T}$  that interacts closely with the DELSEED region ( $\beta$ D394–D400) from  $\beta_{DP}$  and a helix underneath ( $\beta$ D383–M390). Indeed, upon ATP binding to the E-site, the  $\alpha_{E\rightarrow T}$ -loop pushes toward the  $\beta_{DP}$  helix and DELSEED region and moves slightly outward, away from the center, allowing the  $\beta_{DP}$  protrusion to increase and the DP-site to slightly open. On the other hand, the propagation from  $\beta_{E\rightarrow T}$  to  $\alpha_T$  and to  $\beta_T$  was over a comparatively long distance, and the correlation decayed noticeably reaching toward  $\beta_T$ . Since the ADP/ATP binding site mainly locates on the  $\beta$ -subunit, it is reasonable to see that the upstream T-site was affected less than the downstream DP-site by the E-site ATP binding.

#### ATP hydrolysis in T-P-T\* facilitates Pi release from the upstream P-site

To mimic ATP hydrolysis in the T-P-T\* ring (PDB: 1W0J) (51), we enforced the T\*-site to a targeted DP-site confor-

mation, obtained from the crystal structure (PDB: 1E1R) (49). Interestingly, one notices that in the crystal structure of T-P-T\*, the P-site Pi is located around the  $\beta$ P-loop, a marginally stabilized position according to a recent MD study probing the free energy of Pi release (37). It was indicated that the doubly charged Pi group has a tightly bound state located  $\sim 7$  Å inside, whereas the P-loop bound state is a less stabilized intermediate state close to the exit of the Pi release channel.

Since the ring structure T-P-T\* is obtained from bovine MF<sub>1</sub>, the marginally stabilized positioning of Pi in this structure, by itself, suggests a coupling scenario consistent with our proposal for MF<sub>1</sub> (see Fig. S1 C): the Pi release from the P-site of T-P-T\* (to T-E-T\*) has been facilitated right along with the ADP release (from T-DP-T\* to T-P-T\*) upon ATP binding in the upstream site (E-DP-T to T-DP-T\*; see Fig. 1 C, top).

Moreover, we captured in the TMD simulation of the T-P-T\* ring a complete Pi release event from the P-site upstream of the enforced T\*-site. Within 50 ns of the TMD simulation, the protrusion of the T\*-site dropped slightly,



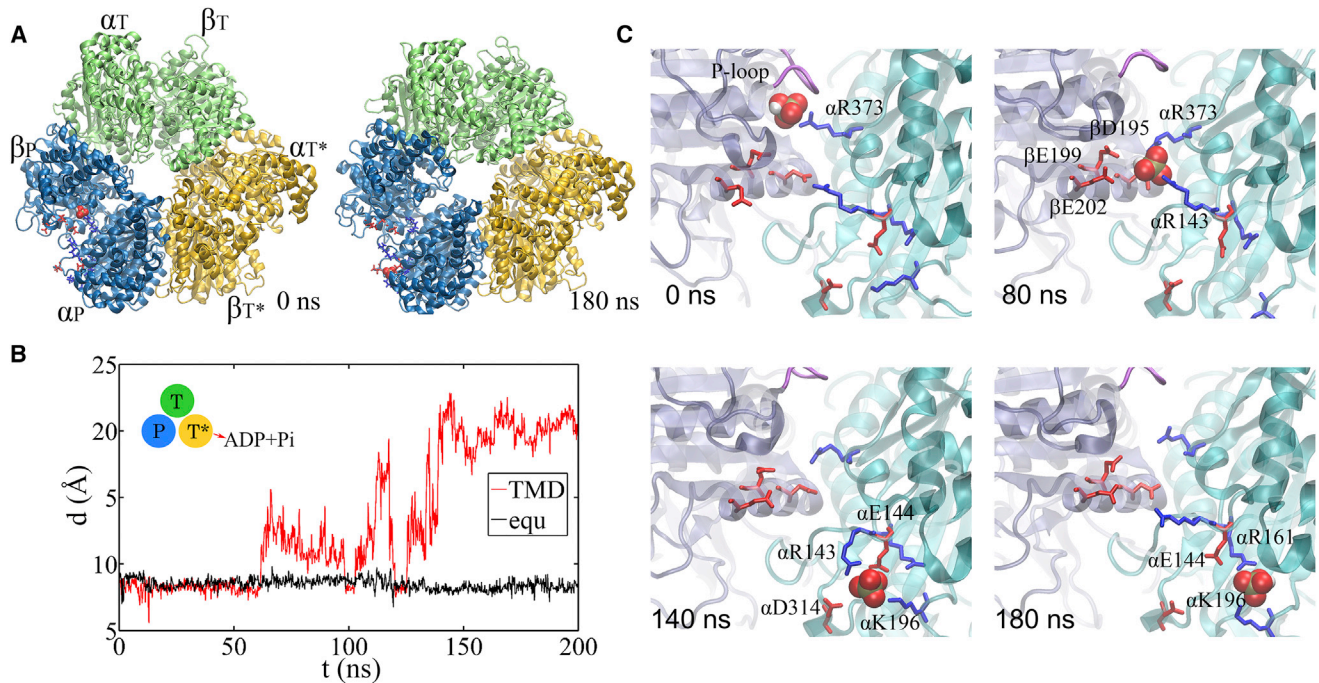


FIGURE 4 TMD simulation enforcing an ATP hydrolysis transition to the T\*-site in the T-P-T\* ring. (A) Top views of the ring at an early and a late stage of the simulation (green, T-site; blue, P-site; yellow, T\*-site). (B) The distance between Pi and an inside reference ( $C\alpha$  of  $\alpha R373$ ) in the TMD and an equilibrium (*equ*) control simulation of the T-P-T\* ring. (C) The full pathway of Pi release captured in the TMD simulation.  $\beta_P$  is colored in ice blue, its P-loop in magenta, and  $\alpha_P$  in cyan. The key charged residues are colored in blue (positively charged) and red (negatively charged). The Pi group (spheres) hopped from the arginine finger  $\alpha R373$  to  $\alpha R143$  (~80 ns), and then to  $\alpha K196$  (~140 ns) and  $\alpha R161$  (~180 ns) before the final release. Three negatively charged residues from  $\beta_P$  (D195, E199, and E202) also helped the Pi release through repulsion. To see this figure in color, go online.

showing a tightening of the site key to the ATP hydrolysis ( $T^* \rightarrow DP$ ). Meanwhile, one notices an up to ~3 Å rise of the  $\beta_P$  protrusion for the P-site (see Fig. 4 A; Fig. S13), indicating an opening response of the P-site within 50 ns that consequently led to the Pi release. The finding that the Pi release was facilitated upon the enforced hydrolysis nicely confirms the prediction from the recent experimental data analyses (28), conducted for BF<sub>1</sub> (thermophilic *Bacillus* PS3).

Remarkably, our TMD simulation demonstrated a complete charge-hopping pathway of the Pi release through three arginine residues and one lysine residue (see Fig. 4 B; Movies S3 and S4), which has not been revealed before. The Pi group was initially positioned through hydrogen bonding with both the P-loop from the  $\beta_P$  subunit and the first arginine finger residue, Arg373, from the  $\alpha_P$  subunit. In response to the enforced hydrolysis transition,  $T^* \rightarrow DP$ , the P-loop from  $\beta_P$  retracted slightly from Pi. Meanwhile, Arg143, the second arginine finger from  $\alpha_P$ , which frequently switched its side chain between Arg373 and Glu144, captured Pi after ~50 ns of the simulation, so that Pi dissociated from Arg373. In addition, three negatively charged residues from the  $\beta_P$  subunit, Asp195, Glu199, and Glu202, helped to repel Pi away from  $\beta_P$ . Later on, Pi was further transferred to Lys196 (~140 ns) and Arg161 (~180 ns) on  $\alpha_P$  and then released fully from the

F<sub>1</sub> ring at the end of the 200 ns TMD simulation. In contrast, in an equilibrium control simulation of the T-P-T\* ring (for 200 ns), Pi was kept stable in association with the P-loop and Arg373, whereas the Arg143 side chain was trapped with Asp314 most of time (see Fig. 4 C; Movie S5).

To understand why the conformational transition  $T^* \rightarrow DP$  impacts the P-site that is upstream to the enforced T\*-site, we examined again the residue-wise correlations on the T-P-T\* ring during the enforced transition (see Fig. 5). In particular, we see that the overall correlation decayed quickly right away from the T\*-site. Nevertheless, one notices that the local region of the P-site correlates well with the T\*-site residues. A close examination shows that the correlation propagates from the hydrolysis site on  $\beta_{T^* \rightarrow DP}$  via an inactive site at the interface of  $\beta_{T^* \rightarrow DP}$  and  $\alpha_P$ , and then extends along a narrow region of a  $\beta$ -sheet structure in the middle part of  $\alpha_P$  ( $\alpha$ Arg164–Arg171,  $\alpha$ Ile345–Leu352, and  $\alpha$ Leu369–Arg373), and finally reaches the P-site at  $\alpha_P$ - $\beta_P$ . The connection with the corresponding residues in  $\alpha_{T^* \rightarrow DP}$  was, however, broken toward the  $\beta_T$  direction due to a gap region right at the  $\alpha_{T^* \rightarrow DP}$ - $\beta_T$  interface, where another inactive site is located (see Fig. 5 C). A movie was made to show the dynamics of the conformation propagation from the T\*-site to the P-site (see Movie S6).

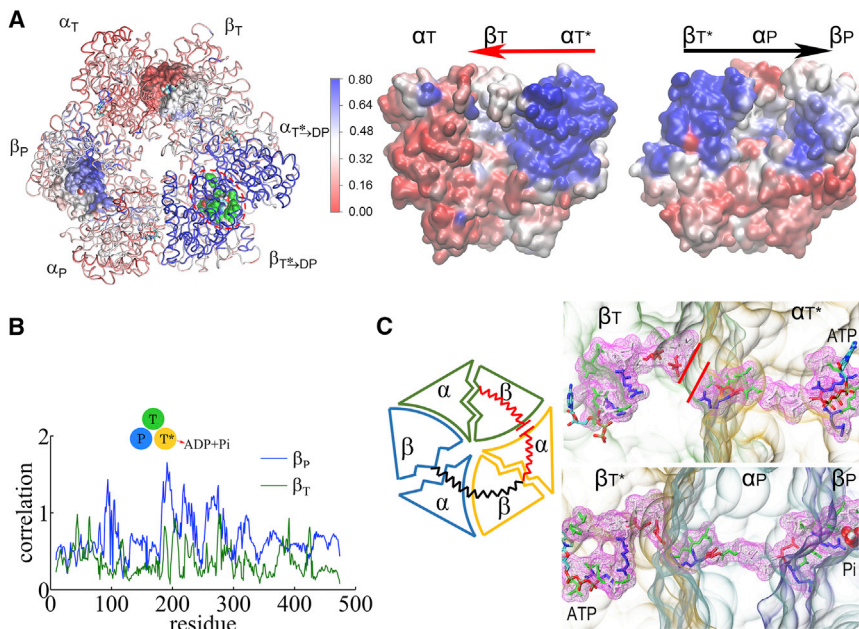


**FIGURE 5** Conformation correlation with the ATP hydrolysis pocket in the TMD simulation of the T-P-T\* ring. (A) Correlation map (left) of the full ring during the enforced T\*→DP transition starting from T-P-T\*, colored according to the correlation values (blue/white/red, high/medium/low) between individual residues and the T\*-site ATP binding/hydrolysis residues (green spheres). An inside side view (right) shows the conformation propagation or correlation from  $\alpha_{T^*} \rightarrow_{DP} \beta_T$  to  $\alpha_T$ , and from  $\beta_{T^*} \rightarrow_{DP} \alpha_P$  to  $\beta_P$ . (B) Residue-wise correlation from  $\beta_P$  (blue) and  $\beta_T$  (green). (C) A close structural view of the connecting residues along the two propagation pathways from  $\alpha_{T^*} \rightarrow_{DP} \beta_T$  to  $\alpha_T$  (top right) and from  $\beta_{T^*} \rightarrow_{DP} \alpha_P$  to  $\beta_P$  (bottom right). A gap region is indicated by two red lines on the former path (top right). The cartoon schematics illustrating the two pathways is shown on the left. To see this figure in color, go online.

#### The first ATP binding opens the next downstream E-site more than the upstream E-site

To investigate whether asymmetrical responses arise on the early tri-site reaction path, we conducted the TMD simulation to a fully empty ring E-E-E (see Figs. S14 and S15; Supporting Material). First, we enforced an E→T transition on one pair of  $\alpha_E$ - $\beta_E$  (blue site) in the E-E-E ring; we then observed trends of mechanical responses similar to those in the E-DP-T configuration: The downstream E-site (yellow site) opened compared to the equilibrium control simulation, whereas the upstream E-site (green site) did not (see Fig. 6 A; Fig. S15). Further calculations on the cross-correlations also show an asymmetrical pattern (Fig. S16). Nevertheless, the three E-sites in the E-E-E ring were not identical (see Fig. 6; Fig. S14), e.g., one of the sites (green site) appears to open more than the other two as its protrusion height and pocket radius stay comparatively large in the equilibrium simulation. Accordingly, we conducted an additional run of the TMD simulation to see if the responses were sensitive to the initial configuration of the E-site. Again, by enforcing an E→T transition to another E-site (green site), the downstream site (now blue) opens more than the upstream site (yellow site), though one would notice that the opening bias appears small and large fluctuations are sampled in the MD simulations (see Figs. S14 and S15). Anyhow, it is also interesting to notice that the yellow E-site, being the downstream site in the first TMD run (see Fig. 6 A), demonstrated a much larger increase of the protrusion height than in the second TMD run, in which it became the upstream site of the enforced ATP binding site. Hence, we concluded that without ligand binding in the neigh-

boring active sites, the asymmetrical responses toward the ATP binding already exist in the ring.

Indeed, the asymmetrical responses triggered by the first ATP binding to the ring can bring a bias in recruiting the second ATP. We found through the KMC simulation that if the second ATP is recruited to the downstream site with a slight bias over the upstream site (e.g., a binding-rate ratio of  $\sim 10$ ), then the reaction intermediate quickly converges to E-T\*-T, and then to E-DP-T (see Fig. 6 C), rather than to the “reversal configurations” T-T\*-E and then T-DP-E. Once the E-DP-T configuration is reached, the chemical cycles repeat, as demonstrated in Fig. 1 C, for both MF<sub>1</sub> and BF<sub>1</sub>.

#### The third ATP binding to the ring destabilizes both neighboring ATP-bound sites

In the KMC simulation, the 3-T configuration in BF<sub>1</sub> was absent due to the coordinated tri-site kinetic, i.e., T-T-T was simply not on the dominant reaction pathway. In contrast, the 3-T configuration in MF<sub>1</sub> needs to be explicitly prohibited to support sequential performance, by reducing the third ATP binding rate ( $\sim 10$  to 100-fold; see Fig. S3 A). In the MD simulation, nevertheless, we enforced a third ATP binding to the E-T\*-T ring (i.e., an intermediate on the MF<sub>1</sub> reaction path) to probe the mechanical (in-)stabilities. We noticed an abnormal increase of the pocket size in the upstream T-site, even though the  $\beta_T$  protrusion dropped (see Figs. S17 and S18). Notably, the bound ATP from the downstream T\*-site released in one of the two TMD simulation trials, though the T\*-site did not open significantly. Hence, the enforced third ATP binding appears unfavorable, as it triggers significant distortions or even destabilizes the bound ATP. In brief, an E-T\*-T ring would

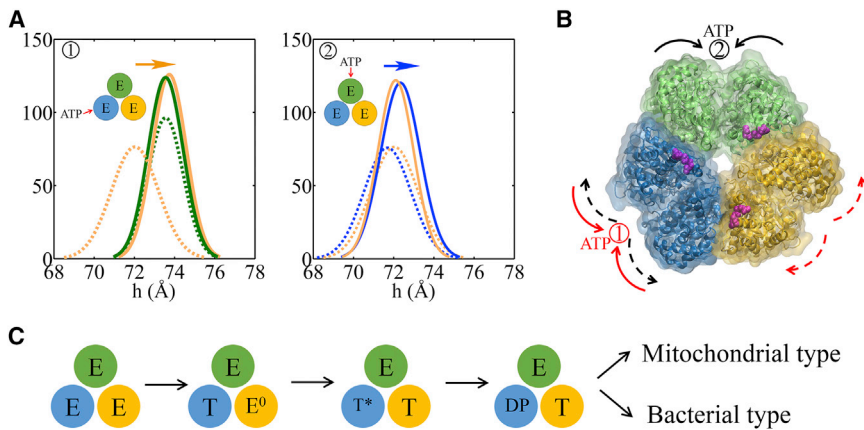


**FIGURE 6** TMD simulations enforcing an E→T transition to one of the E-sites in an empty E-E-E ring. (A) The E-site being forced into a T-site is colored blue (*left*) or green (*right*) in two TMD runs. The  $\beta$ -protrusions from both neighboring E-sites, sampled from the TMD simulation (*solid curves*) and a control equilibrium simulation (*dashed curves*), are shown, with arrows indicating the opening or closing trend. (B) A top view of the E-E-E ring illustrating when one of the E-sites is forced to open, the next/downstream E-site would open in response, whereas the previous/upstream E-site would not. (C) An early reaction pathway starting from an empty F<sub>1</sub>-ring (E-E-E) shows a bias after the first ATP binding. The bias likely facilitates the second ATP binding to the downstream E-site and further leads to the E-DP-T configuration (instead of T-DP-E). To see this figure in color, go online.

either resist the third ATP binding or likely convert to T-E-T\* (rather than T-T\*-E) if the third ATP binding succeeds by chance.

### The TEN simulation induces the asymmetric neighbor-site opening upon ATP binding, as the atomistic TMD does

Note that ATP binding and hydrolysis, along with the induced mechanical responses, involve substantial conformational changes with a characteristic time of up to micro- to milliseconds, which may not be easily sampled by equilibrium atomistic MD. To check whether the accelerated TMD and ensuing responses at the sub-microsecond timescale bear artifacts or capture the essential motions from the original slow dynamics, we also conducted CG simulations of the F<sub>1</sub> ring. We employed the single-bead-per-residue elastic network (EN) description (56), which has been widely used to describe the slow or micro- to millisecond functional domain motions of protein (57–59). To make an easy comparison, we implemented targeted dynamic schemes in the EN model as well and then monitored closely the neighbor site-responses (see [Supporting Material](#)) (53–55). In particular, the forced E→T transition starting from the E-DP-T ring, and that starting from the E-E-E ring, were conducted at the CG level. Upon the E-DP-T to T-DP-T\* transition, the C-terminal  $\beta$ -protrusion of the DP-site increased, indicating an opening, whereas the T-site did not show such an opening (see [Fig. 2 D](#) and [Fig. S19](#)). Upon the E-E-E to E-T-E transition, the asymmetric responses revealed were similar to those triggered by the TMD simulation, in which the downstream site showed opening, whereas the upstream site did not (see [Fig. S20](#)). Hence, regarding the conformational responses due to the inter-subunit coupling on the F<sub>1</sub> ring, agreement between the CG model and the atomistic-level description is obtained. The agreement indicates that the responses under the fast enforcement in the TMD simula-

tions persist when enforcement takes place slowly in the TEN. It also suggests that the conformational responses upon ATP binding or hydrolysis may not be very slow or rate limiting. Instead, it may be the wait for ATP binding or hydrolysis that lasts long enough to be essentially rate limiting in the overall cycle.

### DISCUSSION

To reveal kinetics essentials and structural dynamics mechanisms supporting high coordination of a prototypical ring-shaped NTPase, we investigated computationally the inter-subunit couplings that lead to intrinsic sequential performances of the F<sub>1</sub>-ATPase ring in the absence of the central  $\gamma$  rotor. We first explored which types of inter-subunit couplings are kinetically feasible to allow sequential hydrolysis of the three active sites on the F<sub>1</sub>-ring through the stochastic Monte Carlo simulations. We imposed the primary couplings of the three independent ATP hydrolysis cycles by essentially enhancing the ADP and Pi release rates in one site (i.e., above the uni-site reaction rates) upon a certain neighbor-site ATP binding or hydrolysis event in another site. We found that to support sequential hydrolysis in MF<sub>1</sub>, the ADP release needs to be accelerated  $>\sim 10^5$ -fold upon upstream-site ATP binding to the E-DP-T ring, and similarly for the ensuing Pi release from the same site; in BF<sub>1</sub>, on the other hand, the ADP release needs to be accelerated for above  $\sim 10^3$  fold, while the Pi release can be accelerated either along with the ADP release and/or upon downstream-site ATP hydrolysis in the T-P-T\* ring. To elucidate the physical basis of these kinetically feasible couplings with structural detail, we next performed atomistic TMD simulations to enforce the conformational transition of the ATP binding or hydrolysis to one of the three chemical sites, and we monitored the following mechanical responses from the two neighbor sites. We found essentially the features below from the combined stochastic kinetic and structural dynamics simulations.



**The primary inter-subunit coupling that supports sequential hydrolysis with a directional bias is the ATP-binding-facilitated downstream-site product release, arising from the asymmetrical site opening inherent to the architecture of the trimer-of-heterodimer ring**

Consistently, we found in the atomistic simulation of the E-DP-T ring that the downstream DP-site opens in response to the enforced E-site closing that mimics ATP binding. The site opening was partially characterized by a slight increase of the  $\beta$ -protrusion, the hinge bending angle, and the pocket size of the binding. Further examinations show notable conformational changes along with weakening of the hydrogen-bond network in the peripheral region of the DP-site. All these allosteric impacts induced by the E-site closing would likely facilitate ADP release from the DP-site. When the central  $\gamma$ -rotor was included in the TMD simulation, the  $\beta_{DP}$ -protrusion increase was notably enhanced. Close examination of the cross-correlation of the E-DP-T ring in the absence of the  $\gamma$  rotor shows that the ATP-binding-induced conformational changes propagate asymmetrically from the E-site to the DP- and T-sites via the  $\alpha_E$ - $\beta_{DP}$  and  $\beta_E$ - $\alpha_T$ - $\beta_T$  paths, respectively. The asymmetrical downstream site opening is also preserved upon the induced site closing that mimics the first ATP binding to the empty E-E-E ring. The asymmetrical responses thus appear to be inherent to the architecture of the trimer-of-the-heterodimer ( $\alpha$ - $\beta$ ) ring, in particular, as  $\alpha$ - and  $\beta$ -subunits differ and alternate around the ring, whereas the chemical active site largely locates on  $\beta$ . The inclusion of the  $\gamma$ -rotor into the center of the ring is able to enhance the asymmetrical responses significantly, which either promotes ADP release (and the initial Pi release) or biases the second ATP binding to the downstream site. In particular, the bias for the second ATP binding downstream allows the sequential hydrolysis to proceed directionally (counterclockwise viewed from the C-terminal side).

**Sequential hydrolysis is also supported by proper timing and acceleration of Pi release, which follows ADP release either quickly upon upstream-site ATP binding or later upon downstream-site ATP hydrolysis; Pi release is completed in charge hopping in the simulation**

On the other hand, Pi release can be facilitated via two different mechanisms (see Fig. 1 C), either upstream-site ATP binding that induces ADP release first (MF<sub>1</sub> (18)) or downstream T\*-site ATP hydrolysis (BF<sub>1</sub> (19)). Direct support for the first mechanism comes from the bovine heart MF<sub>1</sub> structure per se (T-P-T\*; PDB: 1W0J) (51), in which the Pi group in the P-site (after ADP release) is located nearby the P-loop, a marginally stabilized state, rather than in the innermost tightly bound state (37). That is,

ATP binding to the ring (from E-DP-T to T-DP-T\*) not only destabilized ADP from the DP-site, but also destabilized the bound Pi, so that Pi moved from the tightly bound state to the marginally stabilized state. The release of Pi thereafter then becomes comparatively easy.

Nevertheless, our equilibrium MD simulation of the T-P-T\* ring was not yet able to capture the Pi release from the P-site within hundreds of nanoseconds. In the equilibrium simulation, the Pi group was associated with the  $\beta$  P-loop as well as the arginine finger  $\alpha$ Arg373. The other arginine finger,  $\alpha$ Arg143, was trapped initially by association with  $\alpha$ Asp314 in the P-site. Nicely, in contrast, a complete Pi-release event was revealed in the TMD simulation, as the P-site mechanistically responded to the enforced hydrolysis in the T\*-site. The P-loop retracted and Arg143 was able to switch occasionally toward Arg373, whereas the three negatively charged residues from  $\beta_P$  also repelled Pi to assist the release. Consequently, the chance that Pi is caught by Arg143 and dissociates from the P-loop increases significantly, and P-loop dissociation becomes critical for further charge hopping, and the final release of Pi.

Compared with the significant open-to-closed conformational changes in the ATP binding site, ATP-hydrolysis-induced conformational changes are rather subtle. We found that the inactive site at the  $\beta_{T^*}$ - $\alpha_P$  interface, along with a  $\beta$ -sheet region on  $\alpha_P$ , actually bridged the mechanistic pathway to propagate the subtle conformational changes from the T\*-site to the P-site, whereas the other way of propagation was broken through the inactive site at the  $\alpha_{T^*}$ - $\beta_T$  interface. In brief, ATP hydrolysis does not generate substantial responses on the protein ring; rather, it triggers local directional conformational propagation via the inactive site and a restricted structural element. Besides, in the T-P-T\* ring, the P-site upstream of the T\*-site is more open and likely much more flexible than the downstream T-site; hence, it appears easier for the mechanical responses to propagate upstream than downstream.

We also found additional couplings or constraints that would help the sequential hydrolysis. An explicit constraint to prevent the third ATP binding to the MF<sub>1</sub> ring (or inhibit the 3-T population) would improve the sequential performance, since the 2-T (T-E-T\*) configuration is on the dominant reaction path of MF<sub>1</sub>. The 2-T configuration can easily turn into 3-T without the constraint, thus interfering with the sequential scheme. The TMD simulation enforcing a third ATP binding to the E-T\*-T ring consistently demonstrated significant destabilization of the neighboring sites. On the other hand, the BF<sub>1</sub> ring achieves sequential performance without the explicit constraint to exclude 3-T, as such a 2-T configuration is not on the dominant reaction path. In addition, we effectively enhanced the ATP hydrolysis rate in the T\*-site, when a second ATP binds to the ring to form a T-site. The rate enhancement in the hydrolysis-ready intermediate T\*-site ensures that hydrolysis takes place sufficiently fast and the site that binds ATP early can hydrolyze



early most of the time. Anyhow, these constraints or couplings were not very stringently imposed, and there was a significant chance that the reactions went off-path to configurations such as 3-T or 2-DP, which might also account for some non-optimal mechanochemical couplings detected early (60).

**Tight coupling is expected between ATP binding and ADP release, and the strength of the coupling can be substantially enhanced by the central  $\gamma$ -rotor; the coupling between ATP hydrolysis and Pi release is notable even in the absence of the  $\gamma$ -rotor**

The rotary sequential hydrolysis of F<sub>1</sub>-ring is basically supported by chemical free energy through the three ATP cycles, which are coordinated with certain phase differences. The coordination also demands free-energy input and dissipation (61). The kinetic rate enhancements in the inter-subunit couplings require lowering activation barriers of the facilitated transitions, e.g., for the hydrolysis product (ADP or Pi) release. For such couplings, either the product binding affinity (or the dissociation constant) is maintained, or the product-rebinding rate remains constant, which requires free-energy compensation from the neighboring unit. For example, to enhance the ADP release rate  $\sim 10^5$ -fold (in MF<sub>1</sub>), it requires up to  $\sim 12$  k<sub>B</sub>T to destabilize the DP-site (with a constant ADP-rebinding rate), and the energy compensation should come from the neighbor-site ATP binding (e.g., by also destabilizing the ATP binding to the T-site). Since the chemical free energy is mostly dissipated through the rotational degree of freedom in the presence of the  $\gamma$ -rotor (62,63), one expects that the  $\gamma$ -rotor would play a significant role in strongly coupling the ATP binding to the next-site ADP release, both structurally and energetically. Current studies indeed show that the  $\beta_{DP}$ -protrusion responds more significantly to the enforced ATP binding in the presence of the  $\gamma$ -rotor than in its absence.

In comparison, the ATP-hydrolysis-facilitated Pi release (rate enhancement  $\sim 10^3$ -fold) appears to require less energetic compensation in the coupling if there is any, so we could actually capture the Pi release event in the absence of the  $\gamma$ -rotor. As such, we infer that the central  $\gamma$ -rotor dictates the inter-subunit coupling more significantly in the ATP binding step than in the ATP hydrolysis step, which leads to stronger inter-subunit couplings or higher coordination in the original F<sub>1</sub>-ATPase with the rotor than in the stator ring only. As a matter of fact, considering the recent MD studies on the  $\gamma$ -shaft rotation and the Pi release (37), together with our current simulation results, we suggest that the initial stage of the Pi release can also be facilitated by the  $\gamma$ -shaft rotation that accompanies the ATP binding and the ADP release. Complete Pi release can be further promoted by the neighbor-site ATP hydrolysis in the bacterial F<sub>1</sub>, which can couple with the additional  $\gamma$ -shaft rotation.

According to our study, one can further tune the inter-subunit coupling kinetics to allow a significant increase in the overall cycling rate of F<sub>1</sub>, approaching experimentally measured values for the full F<sub>1</sub> system with the rotor (see Tables S3 and S4). Hence, one can see that the rotor effectively plays a role in strengthening and further modulating the inter-subunit couplings on the ring, and consequently in promoting the overall hydrolysis rate. Based on current work, it would be promising to determine how exactly the central  $\gamma$ -rotor contributes to the F<sub>1</sub> inter-subunit coordination for the respective steps of ATP binding and hydrolysis. Indeed, the ATP binding and hydrolysis transitions, along with their coordination in the ring assembly, have only been phenomenologically modeled in current work, and they deserve more substantial investigation in future work.

## CONCLUSIONS

Combining stochastic simulations of tri-site chemical kinetics of the F<sub>1</sub> stator ring with targeted atomistic MD and coarse-grained EN simulations, we inferred the most crucial inter-subunit couplings leading to sequential hydrolysis on the F<sub>1</sub> ring: ATP binding facilitates ADP release from a downstream DP-site, along with Pi release from the same site, whereas complete Pi release can be further facilitated by ATP hydrolysis downstream. The couplings come from asymmetrical neighbor-site opening/loosening upon current site closing/tightening produced by the ATP binding/hydrolysis. The dominant conformational asymmetry, demonstrated upon ATP binding, appears to be embedded in the trimer-of-heterodimer ring, owing largely to the alternating arrangement of  $\alpha$ - and  $\beta$ -subunits. Additionally, a minor structural dynamics asymmetry is revealed upon subtle conformational transition under ATP hydrolysis, which impacts the neighbor sites differently via subtle structural variations. The mechanistic propagation around the ring is therefore modulated also by the ligand (ATP, ADP, or Pi) bound status in the neighboring sites. Furthermore, preventing a third ATP from binding to the assembled ring, as well as allowing a hydrolysis-ready intermediate in the ring to have an elevated hydrolysis rate, also supports the sequential hydrolysis on the F<sub>1</sub> ring. Though the overall cycling rate in our simulation of the bacterial F<sub>1</sub> ring matches with the experimental detection of the rotor-less system, it should be noted that the full F<sub>1</sub> in the presence of the rotor rotates and cycles much faster, revealing a central role played by the rotor in enhancing inter-subunit coupling on the ring. The large discrepancy between the cycling rates of mitochondrial and bacterial species of F<sub>1</sub> in the rotor-less case does not necessarily show in the presence of the rotor, indicating further inter-subunit modulation from the rotor. It would be highly interesting to pursue whether comparable coupling scenarios apply to evolutionarily connected ring-shaped protein enzymes working on a central substrate of protein or nucleic acid.

## SUPPORTING MATERIAL

Supporting Materials and Methods, twenty figures, four tables, and six movies are available at [http://www.biophysj.org/biophysj/supplemental/S0006-3495\(17\)30874-3](http://www.biophysj.org/biophysj/supplemental/S0006-3495(17)30874-3).

## AUTHOR CONTRIBUTIONS

J.Y. designed the research. L.D. and H.F. performed the research. L.D. and H.F. analyzed the data. J.Y., H.F., and L.D. wrote the article.

## ACKNOWLEDGMENTS

This work is supported by grants from the National Natural Science Foundation of China (NSFC) (11635002) and NSAF (U153040). H.F. has been supported by Japan Society for the Promotion of Science KAKENHI grant no. JP16K05518. We acknowledge computational support from the Beijing Computational Science Research Center (CSRC) and the Special Program for Applied Research on Super Computation of the NSFC-Guangdong Joint Fund (the second phase) under grant no. U1501501.

## SUPPORTING CITATIONS

References (64–66) appear in the [Supporting Material](#).

## REFERENCES

- Liu, S., G. Chistol, and C. Bustamante. 2014. Mechanical operation and intersubunit coordination of ring-shaped molecular motors: insights from single-molecule studies. *Biophys. J.* 106:1844–1858.
- Iino, R., and H. Noji. 2013. Intersubunit coordination and cooperativity in ring-shaped NTPases. *Curr. Opin. Struct. Biol.* 23:229–234.
- Lyubimov, A. Y., M. Strycharska, and J. M. Berger. 2011. The nuts and bolts of ring-translocase structure and mechanism. *Curr. Opin. Struct. Biol.* 21:240–248.
- Enemark, E. J., and L. Joshua-Tor. 2008. On helicases and other motor proteins. *Curr. Opin. Struct. Biol.* 18:243–257.
- Singleton, M. R., M. S. Dillingham, and D. B. Wigley. 2007. Structure and mechanism of helicases and nucleic acid translocases. *Annu. Rev. Biochem.* 76:23–50.
- Boyer, P. D. 1989. A perspective of the binding change mechanism for ATP synthesis. *FASEB J.* 3:2164–2178.
- Hutton, R. L., and P. D. Boyer. 1979. Subunit interaction during catalysis. Alternating site cooperativity of mitochondrial adenosine triphosphatase. *J. Biol. Chem.* 254:9990–9993.
- Leslie, A. G., and J. E. Walker. 2000. Structural model of F<sub>1</sub>-ATPase and the implications for rotary catalysis. *Philos. Trans. R. Soc. Lond. B Biol. Sci.* 355:465–471.
- Boyer, P. D. 1993. The binding change mechanism for ATP synthase—some probabilities and possibilities. *Biochim. Biophys. Acta.* 1140:215–250.
- Abrahams, J. P., A. G. W. Leslie, ..., J. E. Walker. 1994. Structure at 2.8 Å resolution of F<sub>1</sub>-ATPase from bovine heart mitochondria. *Nature.* 370:621–628.
- Noji, H., R. Yasuda, ..., K. Kinosita, Jr. 1997. Direct observation of the rotation of F<sub>1</sub>-ATPase. *Nature.* 386:299–302.
- Adachi, K., K. Oiwa, ..., K. Kinosita, Jr. 2007. Coupling of rotation and catalysis in F<sub>1</sub>-ATPase revealed by single-molecule imaging and manipulation. *Cell.* 130:309–321.
- Furuike, S., M. D. Hossain, ..., K. Kinosita, Jr. 2008. Axle-less F<sub>1</sub>-ATPase rotates in the correct direction. *Science.* 319:955–958.
- Hossain, M. D., S. Furuike, ..., K. Kinosita, Jr. 2008. Neither helix in the coiled coil region of the axle of F<sub>1</sub>-ATPase plays a significant role in torque production. *Biophys. J.* 95:4837–4844.
- Kohori, A., R. Chiwata, ..., K. Kinosita, Jr. 2011. Torque generation in F<sub>1</sub>-ATPase devoid of the entire amino-terminal helix of the rotor that fills half of the stator orifice. *Biophys. J.* 101:188–195.
- Chiwata, R., A. Kohori, ..., K. Kinosita, Jr. 2014. None of the rotor residues of F<sub>1</sub>-ATPase are essential for torque generation. *Biophys. J.* 106:2166–2174.
- Uchihashi, T., R. Iino, ..., H. Noji. 2011. High-speed atomic force microscopy reveals rotary catalysis of rotorless F<sub>1</sub>-ATPase. *Science.* 333:755–758.
- Suzuki, T., K. Tanaka, ..., M. Yoshida. 2014. Chemomechanical coupling of human mitochondrial F<sub>1</sub>-ATPase motor. *Nat. Chem. Biol.* 10:930–936.
- Watanabe, R., and H. Noji. 2014. Timing of inorganic phosphate release modulates the catalytic activity of ATP-driven rotary motor protein. *Nat. Commun.* 5:3486.
- Senior, A. E. 1992. Catalytic sites of *Escherichia coli* F<sub>1</sub>-ATPase. *J. Bioenerg. Biomembr.* 24:479–484.
- Grubmeyer, C., R. L. Cross, and H. S. Penefsky. 1982. Mechanism of ATP hydrolysis by beef heart mitochondrial ATPase. Rate constants for elementary steps in catalysis at a single site. *J. Biol. Chem.* 257:12092–12100.
- Hauk, G., and J. M. Berger. 2016. The role of ATP-dependent machines in regulating genome topology. *Curr. Opin. Struct. Biol.* 36:85–96.
- Lísal, J., and R. Tuma. 2005. Cooperative mechanism of RNA packaging motor. *J. Biol. Chem.* 280:23157–23164.
- Yu, J., J. Moffitt, ..., G. Oster. 2010. Mechanochemistry of a viral DNA packaging motor. *J. Mol. Biol.* 400:186–203.
- Thomsen, N. D., M. R. Lawson, ..., J. M. Berger. 2016. Molecular mechanisms of substrate-controlled ring dynamics and substepping in a nucleic acid-dependent hexameric motor. *Proc. Natl. Acad. Sci. USA.* 113:E7691–E7700.
- Adolfson, R., and E. N. Moudrianakis. 1976. Binding of adenine nucleotides to the purified 13S coupling factor of bacterial oxidative phosphorylation. *Arch. Biochem. Biophys.* 172:425–433.
- Yu, J. 2014. Coordination and Control Inside Simple Biomolecular Machines. In *Protein Conformational Dynamics, Advances in Experimental Medicine and Biology*. K. Han, editor. Springer International, pp. 353–383.
- Li, C.-B., H. Ueno, ..., T. Komatsuzaki. 2015. ATP hydrolysis assists phosphate release and promotes reaction ordering in F<sub>1</sub>-ATPase. *Nat. Commun.* 6:10223.
- Wang, H., and G. Oster. 1998. Energy transduction in the F<sub>1</sub> motor of ATP synthase. *Nature.* 396:279–282.
- Böckmann, R. A., and H. Grubmüller. 2002. Nanoseconds molecular dynamics simulation of primary mechanical energy transfer steps in F<sub>1</sub>-ATP synthase. *Nat. Struct. Biol.* 9:198–202.
- Dittrich, M., S. Hayashi, and K. Schulten. 2003. On the mechanism of ATP hydrolysis in F<sub>1</sub>-ATPase. *Biophys. J.* 85:2253–2266.
- Gao, Y. Q., W. Yang, and M. Karplus. 2005. A structure-based model for the synthesis and hydrolysis of ATP by F<sub>1</sub>-ATPase. *Cell.* 123:195–205.
- Koga, N., and S. Takada. 2006. Folding-based molecular simulations reveal mechanisms of the rotary motor F<sub>1</sub>-ATPase. *Proc. Natl. Acad. Sci. USA.* 103:5367–5372.
- Gaspard, P., and E. Gerritsma. 2007. The stochastic chemomechanics of the F<sub>1</sub>-ATPase molecular motor. *J. Theor. Biol.* 247:672–686.
- Mukherjee, S., and A. Warshel. 2011. Electrostatic origin of the mechanochemical rotary mechanism and the catalytic dwell of F<sub>1</sub>-ATPase. *Proc. Natl. Acad. Sci. USA.* 108:20550–20555.
- Ito, Y., T. Yoshidome, ..., M. Ikeguchi. 2013. Molecular dynamics simulations of yeast F<sub>1</sub>-ATPase before and after 16° rotation of the  $\gamma$  subunit. *J. Phys. Chem. B.* 117:3298–3307.

37. Okazaki, K., and G. Hummer. 2013. Phosphate release coupled to rotary motion of F<sub>1</sub>-ATPase. *Proc. Natl. Acad. Sci. USA.* 110:16468–16473.
38. Okazaki, K., and G. Hummer. 2015. Elasticity, friction, and pathway of  $\gamma$ -subunit rotation in F<sub>o</sub>F<sub>1</sub>-ATP synthase. *Proc. Natl. Acad. Sci. USA.* 112:10720–10725.
39. Schlitter, J., M. Engels, and P. Krüger. 1994. Targeted molecular dynamics: a new approach for searching pathways of conformational transitions. *J. Mol. Graph.* 12:84–89.
40. Cheng, X., H. Wang, ..., J. A. McCammon. 2006. Targeted molecular dynamics study of C-loop closure and channel gating in nicotinic receptors. *PLOS Comput. Biol.* 2:e134.
41. Ovchinnikov, V., and M. Karplus. 2012. Analysis and elimination of a bias in targeted molecular dynamics simulations of conformational transitions: application to calmodulin. *J. Phys. Chem. B.* 116:8584–8603.
42. Watanabe, R., R. Iino, and H. Noji. 2010. Phosphate release in F<sub>1</sub>-ATPase catalytic cycle follows ADP release. *Nat. Chem. Biol.* 6:814–820.
43. Bilyard, T., M. Nakanishi-Matsui, ..., R. M. Berry. 2012. High-resolution single-molecule characterization of the enzymatic states in *Escherichia coli* F<sub>1</sub>-ATPase. *Philos. Trans. R. Soc. Lond. B Biol. Sci.* 368:20120023.
44. Chatterjee, A., and D. G. Vlachos. 2007. An overview of spatial microscopic and accelerated kinetic Monte Carlo methods. *J. Comput. Aided Mater. Des.* 14:253–308.
45. Nelson, M. T., W. Humphrey, ..., K. Schulten. 1996. NAMD: a parallel, object-oriented molecular dynamics program. *Int. J. High Perform. Comput. Appl.* 10:251–268.
46. MacKerell, A. D., D. Bashford, ..., M. Karplus. 1998. All-atom empirical potential for molecular modeling and dynamics studies of proteins. *J. Phys. Chem. B.* 102:3586–3616.
47. Foloppe, N., and A. D. MacKerell, Jr. 2000. All-atom empirical force field for nucleic acids: I. Parameter optimization based on small molecule and condensed phase macromolecular target data. *J. Comput. Chem.* 21:86–104.
48. Berendsen, H. J. C., D. van der Spoel, and R. van Drunen. 1995. GROMACS: a message-passing parallel molecular dynamics implementation. *Comput. Phys. Commun.* 91:43–56.
49. Braig, K., R. I. Menz, ..., J. E. Walker. 2000. Structure of bovine mitochondrial F<sub>1</sub>-ATPase inhibited by Mg<sup>2+</sup> ADP and aluminium fluoride. *Structure.* 8:567–573.
50. Bowler, M. W., M. G. Montgomery, ..., J. E. Walker. 2007. Ground state structure of F<sub>1</sub>-ATPase from bovine heart mitochondria at 1.9 Å resolution. *J. Biol. Chem.* 282:14238–14242.
51. Kagawa, R., M. G. Montgomery, ..., J. E. Walker. 2004. The structure of bovine F<sub>1</sub>-ATPase inhibited by ADP and beryllium fluoride. *EMBO J.* 23:2734–2744.
52. Darden, T., D. York, and L. Pedersen. 1993. Particle mesh Ewald: An N<sup>+</sup> log(N) method for Ewald sums in large systems. *J. Chem. Phys.* 98:10089–10092.
53. Flechsig, H., and A. S. Mikhailov. 2010. Tracing entire operation cycles of molecular motor hepatitis C virus helicase in structurally resolved dynamical simulations. *Proc. Natl. Acad. Sci. USA.* 107:20875–20880.
54. Togashi, Y., and A. S. Mikhailov. 2007. Nonlinear relaxation dynamics in elastic networks and design principles of molecular machines. *Proc. Natl. Acad. Sci. USA.* 104:8697–8702.
55. Togashi, Y., T. Yanagida, and A. S. Mikhailov. 2010. Nonlinearity of mechanochemical motions in motor proteins. *PLOS Comput. Biol.* 6:e1000814.
56. Bahar, I., A. R. Atilgan, and B. Erman. 1997. Direct evaluation of thermal fluctuations in proteins using a single-parameter harmonic potential. *Fold. Des.* 2:173–181.
57. Bahar, I., T. R. Lezon, ..., E. Eyal. 2010. Global dynamics of proteins: bridging between structure and function. *Annu. Rev. Biophys.* 39:23–42.
58. Cui, Q., and I. Bahar. 2005. Normal Mode Analysis: Theory and Applications to Biological and Chemical Systems. Chapman and Hall/CRC, London/Boca Raton, FL.
59. Zheng, W., and S. Doniach. 2003. A comparative study of motor-protein motions by using a simple elastic-network model. *Proc. Natl. Acad. Sci. USA.* 100:13253–13258.
60. Rondelez, Y., G. Tresset, ..., H. Noji. 2005. Highly coupled ATP synthesis by F<sub>1</sub>-ATPase single molecules. *Nature.* 433:773–777.
61. Cao, Y., H. Wang, ..., Y. Tu. 2015. The free energy cost of accurate biochemical oscillations. *Nat. Phys.* 11:772–778.
62. Toyabe, S., T. Okamoto, ..., E. Muneyuki. 2010. Nonequilibrium energetics of a single F<sub>1</sub>-ATPase molecule. *Phys. Rev. Lett.* 104:198103.
63. Kawaguchi, K., S. Sasa, and T. Sagawa. 2014. Nonequilibrium dissipation-free transport in F<sub>1</sub>-ATPase and the thermodynamic role of asymmetric allostereism. *Biophys. J.* 106:2450–2457.
64. Antes, I., D. Chandler, ..., G. Oster. 2003. The unbinding of ATP from F<sub>1</sub>-ATPase. *Biophys. J.* 85:695–706.
65. Hornak, V., R. Abel, ..., C. Simmerling. 2006. Comparison of multiple Amber force fields and development of improved protein backbone parameters. *Proteins.* 65:712–725.
66. Yang, Y., Q. Cui, and N. Sahai. 2010. How does bone sialoprotein promote the nucleation of hydroxyapatite? A molecular dynamics study using model peptides of different conformations. *Langmuir.* 26:9848–9859.